

Calibration and Validation of the TEMPEST-D CubeSat Radiometer

Wesley Berg¹, *Member, IEEE*, Shannon T. Brown¹, *Senior Member, IEEE*, Boon H. Lim,
Steven C. Reising¹, *Senior Member, IEEE*, Yuriy Goncharenko, *Member, IEEE*,
Christian D. Kummerow¹, Todd C. Gaier, and Sharmila Padmanabhan¹, *Member, IEEE*

Abstract—Temporal Experiment for Storms and Tropical Systems—Demonstration (TEMPEST-D) is a 6U CubeSat satellite with a cross-track scanning millimeter-wave radiometer measuring at five frequencies from 87 to 181 GHz. It employs a direct-detection architecture with InP HEMT monolithic microwave integrated circuit (MMIC) low-noise amplifiers and related new technologies. An end-to-end two-point external calibration is performed every 2-s rotation of the scanning mirror, based on observations of the cosmic microwave background and an internal blackbody calibration target, with three thermistors to monitor the target physical temperature. Corrections for antenna pattern effects and cross-scan biases based on prelaunch measured values were updated using data from an on-orbit calibration pitch maneuver. Validation of the observed brightness temperatures (T_B) is performed by comparing to coincident nonprecipitating ocean observations from five well-calibrated on-orbit instruments, including Global Precipitation Measurement (GPM) mission Microwave Imager (GMI) and four Microwave Humidity Sounder (MHS) sensors on board NOAA-19, MetOp-A, MetOp-B, and MetOp-C satellites. Absolute calibration accuracy is within 1 K for all channels, well within the 4-K requirement. Calibration precision, or stability over time, is within 0.6 K for all channels, also well within the 2-K requirement. The intrinsic noise of TEMPEST-D is lower than MHS, resulting in similar on-orbit noise equivalent differential temperatures (NEDTs), even though TEMPEST-D has a much shorter integration time of 5 ms as compared to 18 ms for MHS. As a result, although the TEMPEST-D radiometer is substantially smaller, lower power, and lower cost than similar current operational radiometers, it has comparable or better performance in terms of instrument noise, calibration accuracy, and calibration stability or precision.

Index Terms—Calibration, CubeSats, microwave radiometry, passive microwave remote sensing, satellite, Temporal Experiment for Storms and Tropical Systems—Demonstration (TEMPEST-D), validation.

Manuscript received March 10, 2020; revised July 2, 2020; accepted August 13, 2020. This work was supported by the National Aeronautics and Space Administration (NASA) under Grant NNX15AP56G. (*Corresponding author: Wesley Berg.*)

Wesley Berg and Christian D. Kummerow are with the Department of Atmospheric Science, Colorado State University, Fort Collins, CO 80523 USA (e-mail: berg@atmos.colostate.edu; kummerow@atmos.colostate.edu).

Shannon T. Brown, Boon H. Lim, Todd C. Gaier, and Sharmila Padmanabhan are with NASA Jet Propulsion Laboratory, California Institute of Technology, Pasadena, CA 91109 USA (e-mail: shannon.t.brown@jpl.nasa.gov; boon.h.lim@jpl.nasa.gov; todd.c.gaier@jpl.nasa.gov; sharmila.padmanabhan@jpl.nasa.gov).

Steven C. Reising and Yuriy Goncharenko are with the Department of Electrical Engineering, Colorado State University, Fort Collins, CO 80523 USA (e-mail: steven.reising@colostate.edu; yuriy.goncharenko@colostate.edu).

Color versions of one or more of the figures in this article are available online at <http://ieeexplore.ieee.org>.

Digital Object Identifier 10.1109/TGRS.2020.3018999

0196-2892 © 2020 IEEE. Personal use is permitted, but republication/redistribution requires IEEE permission.
See <https://www.ieee.org/publications/rights/index.html> for more information.

I. INTRODUCTION

THE Temporal Experiment for Storms and Tropical Systems—Demonstration (TEMPEST-D) is a 6U CubeSat with a cross-track scanning millimeter-wave radiometer operating at five frequencies centered near 87, 164, 174, 178, and 181 GHz [1]. The TEMPEST-D channels were selected for their sensitivity to water vapor, cloud water, and cloud ice to meet science requirements for the originally proposed TEMPEST constellation mission. The TEMPEST mission concept is a series of five identical satellites flying in formation observing at five-minute intervals to provide information on the temporal evolution of storms. The single TEMPEST-D satellite is a technology demonstration mission to reduce risk and demonstrate measurement capabilities for 6U-Class satellite constellations for Earth Science. It was launched on a commercial resupply mission to the International Space Station (ISS) on May 18, 2018, and deployed into orbit on July 13, 2018.

The requirements for the TEMPEST-D mission include demonstrating calibration accuracy within 4 K and calibration precision within 2 K for at least two of the five channels. Detailed information on TEMPEST-D instrument specifications and prelaunch calibration are available in [1] and [2]. The similarity of TEMPEST-D measurement characteristics to those of the well-calibrated operational Microwave Humidity Sounder (MHS) instruments on board NOAA-18/19 and MetOp-A/B/C makes it possible to verify these requirements on orbit.

II. INSTRUMENT OVERVIEW

The TEMPEST-D instrument has a scanning offset paraboloid reflector illuminated by a single fixed feed horn and diplexer covering the frequency range from 87 to 181 GHz. The 87- and 164–181-GHz bands are divided into the diplexer as part of the feed horn assembly and then input to individual total-power direct-detection receivers based on InP HEMT monolithic microwave integrated circuit (MMIC) low-noise amplifiers. The frequencies for the five channels are defined using RF bandpass filters. The analog RF signal is detected using a detector diode and then digitized. The sensor contains a blackbody calibration target located near the zenith direction of the scan. A cut-out in the spacecraft frame provides a clear view of cold space to provide the second calibration source. Both calibration sources are viewed through the same reflector every 2 s at the nominal reflector rotation rate of 30 r/min.

The brightness temperature (T_B) for each channel is produced in two steps. First, the TEMPEST-D calibrated antenna temperature (T_A) is computed from the raw voltage using a standard two-point calibration technique referenced to the ambient blackbody calibration target and cold sky view. T_B is then computed from T_A by accounting for the feed-horn spillover outside of the reflector. To compute T_A , the radiometer gain and offset are computed once per scan. The total integration time for each calibration source is approximately 100 ms, or 20 samples at the nominal 5-ms integration period, during each scan. The usable angular extent for each calibration source was defined prelaunch and subsequently refined on orbit. The 0.5-Hz calibration measurements are averaged over multiple scans along the track to reduce noise, with a configurable averaging window currently set to 15 scans. To compute T_A , the time series of calibration samples is interpolated to the time of each antenna measurement.

To compute T_B , the small scan-position-dependent feed horn spill-over contribution to the T_A is removed. This is a consequence of slight asymmetries in the feed pattern as well as asymmetries in the residual scene, producing a variable amount of spill-over thermal emission as the reflector rotates. This is modeled as

$$T_B = \frac{1}{\alpha(\varphi)}(T_A - (1 - \alpha(\varphi))T_\alpha) \quad (1)$$

where $\alpha(\varphi)$ is the spillover as a function of scan angle φ and T_α is the effective spillover T_B .

III. PRELAUNCH INSTRUMENT CHARACTERIZATION

Prior to launch, measurements were performed to characterize various aspects of the instrument, including the radiometric properties over the expected temperature range (e.g., gain, offset, and noise), end-to-end spectral response, and antenna patterns for each channel. For cross-calibration (i.e., validation), the spectral response knowledge is among the most important parameters. Fig. 1 shows the spectral response for the five TEMPEST-D channels as normalized power versus frequency. The dashed line indicates the filter response, while the solid line provides a more accurate characterization of the spectral response based on an end-to-end radiometer response measurement. The end-to-end spectral response includes the individual component spectral responses of the reflector, low-noise amplifiers, power divider, filter, detector, and the standing waves between them. Accurate measurements of the instrument spectral response are critical for radiative transfer model simulations used to validate the instrument calibration as well as for science applications including geophysical retrievals and data assimilation.

The spectral response patterns shown in Fig. 1 indicate significant deviations from the standard “boxcar” response characterization based solely on center frequency and bandwidth. This is particularly impactful when simulating channels near the 183.31-GHz water vapor line, since variations in atmospheric transmittance as a function of frequency are not linear. Accurate measurements of the instrument spectral response are particularly important for TEMPEST-D due to

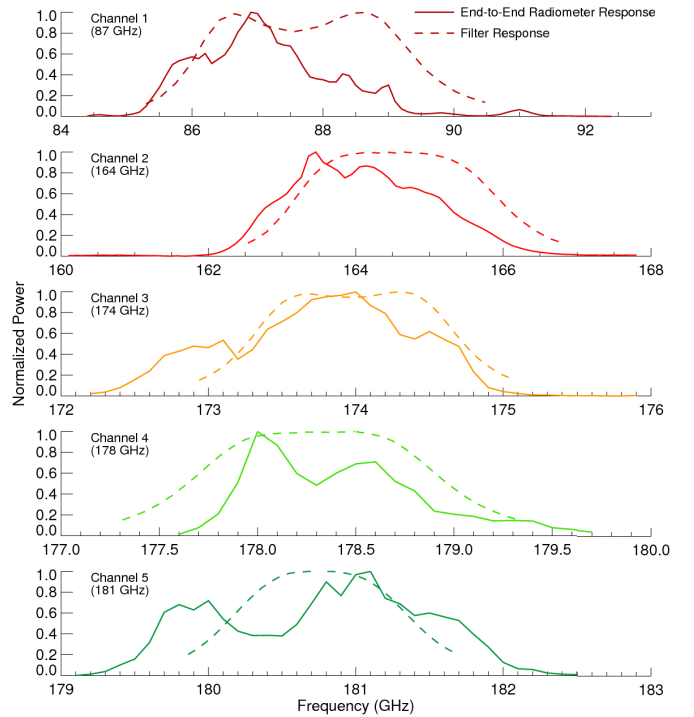


Fig. 1. Spectral response weighting functions for the TEMPEST-D channels. The dashed lines indicate the filter response, while the solid lines show the end-to-end radiometer response.

the effect of manufacturing variations for miniaturized components. The small size of the complete 6U-Class satellite with the radiometer integrated into a mechanical model of the spacecraft bus made possible end-to-end measurements, providing the more accurate spectral response weighting functions used for validation and science applications.

Measurements of the antenna patterns performed prior to launch were used to develop the antenna pattern corrections to convert the calibrated T_A to T_B [2]. The prelaunch measurements indicated that the spill-over contribution would be less than 0.5 K, which was subsequently verified on-orbit. Adjustments to the prelaunch measured values were made based on an analysis of data from on-orbit calibration maneuvers.

IV. POSTLAUNCH INSTRUMENT CHARACTERIZATION

The TEMPEST-D instrument began nominal operations on September 5, 2018. Primary instrument characterization objectives after launch included refining the angular ranges used for the blackbody calibration target and cold sky view, as well as tuning the antenna spill-over correction.

The top of Fig. 2 shows a schematic with the approximate locations of the blackbody calibration target, cold sky, and Earth view sectors during a full rotation of the antenna. The angular ranges of the blackbody calibration target and cold sky view were refined on-orbit by analyzing the mean and standard deviation of the T_B as a function of scan angle, as depicted in the bottom of Fig. 2. The optimal angular region was determined based on the flatness of the mean relative to the center position of the calibration source and the standard

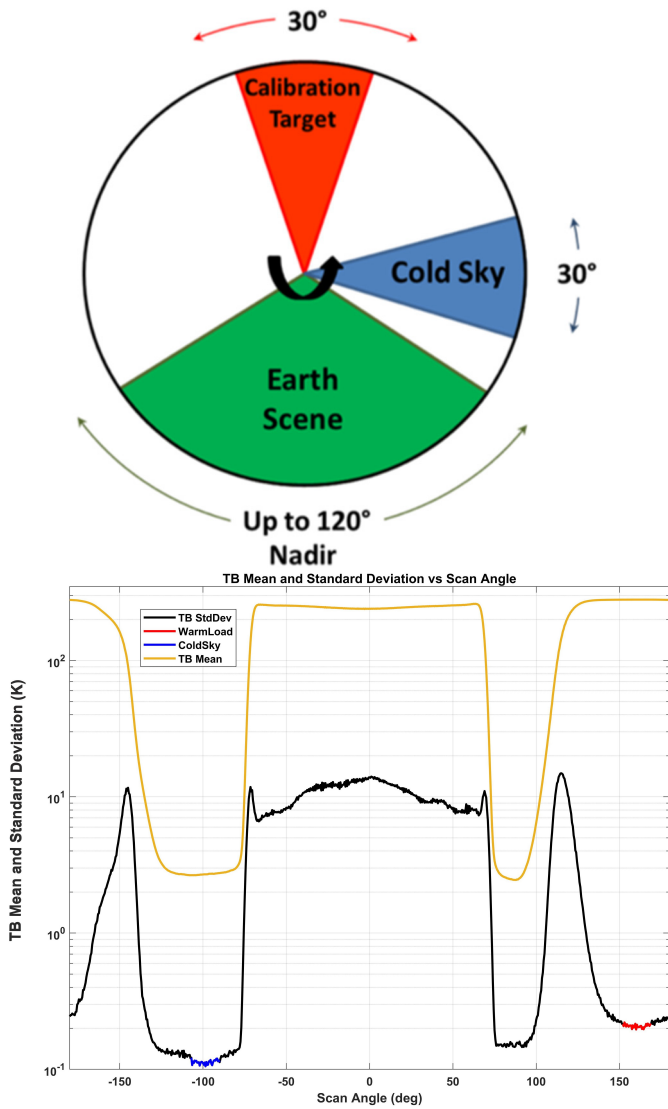


Fig. 2. (Top) Schematic of the relative positions of the Earth view, calibration target, and cold-sky view sectors within the 360° rotation of the TEMPEST-D antenna. (Bottom) Mean and standard deviation of T_B as a function of the scan angle, where 0° corresponds to the nadir direction. The selected calibration target and cold sky angular ranges are shown in red and blue, respectively. The useable Earth view portion of the scan is in the center between $\pm 60^\circ$.

deviation relative to the noise equivalent differential temperature (NEDT). The boundaries for the blackbody calibration target were set from 152° to 169°, and the boundaries for the cold sky view were set from -107° to -90°, where 0° corresponds to the nadir pointing direction.

A special calibration maneuver was performed to estimate the spill-over fraction on orbit. The spacecraft was pitched over a complete 360° at the rate of 14.5°/min so that the reflector scanned across the uniform cold sky over the angular range normally used to observe the Earth. During the pitch maneuver, the data were calibrated using one-point calibration based on the blackbody calibration target temperature to track the gain variation. The receiver noise temperature was parameterized as a linear function of the receiver's physical temperature using one orbit of two-point calibration data

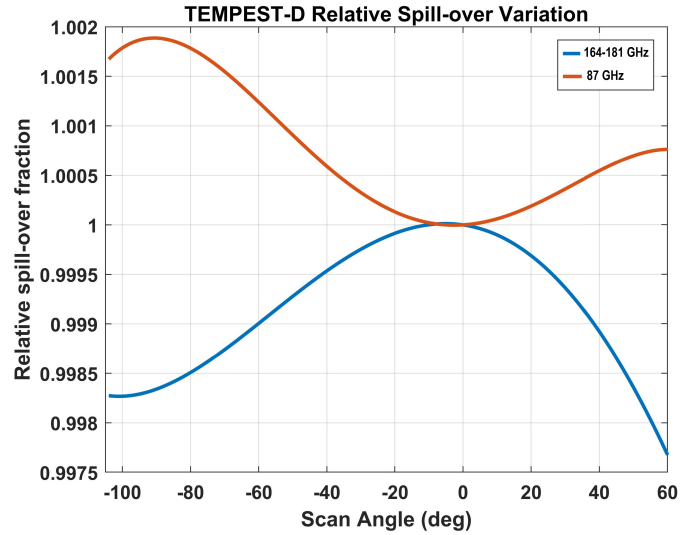


Fig. 3. Relative spillover variation for the two TEMPEST-D bands as a function of scan angle. Scan angles from -60° to 60° correspond to the Earth view, while the cut-off for the cold-sky view used for calibration corresponds to approximately -100° .

adjacent to the pitch maneuver data. Inspection of the data from the pitch maneuver showed that the variations in T_A at a given scan angle flattened after the boresight was 10° above the horizon, suggesting that the contribution of the Earth was minimal beyond this point. This is expected since the spacecraft structure blocks the Earth in this orientation.

When the pitch angle exceeded 150°, T_A were averaged as a function of the scan angle to estimate the relative spill-over variation over the scan. The spill-over temperature, T_α in (1), is approximated by the blackbody calibration target's average thermistor temperature, which tracks the physical temperature of the instrument. In addition, most of the reflected spill-over radiation inside the spacecraft ultimately terminates in the absorber. Equation (1) is inverted to solve for $\alpha(\varphi)$ by setting T_B to the cosmic microwave background brightness and using the measured T_A and T_α . The relative spillover is parameterized using a fourth-order polynomial as a function of scan angle (φ), as expressed in (2) and shown in Fig. 3 for the Earth view sector (-60° to 60°) relative to the cold-sky calibration view (at approximately -100°). The relative spillover shown in Fig. 3 is normalized to 1.0. Based on the values shown in Fig. 3, for a 200-K scene, the spill-over contribution is less than 0.5 K, even in the worst case at an extreme 60° scan angle. The 164–181-GHz channels have nearly identical spill-over values and are thus all indicated by the blue line in Fig. 3 and use the same spillover parameterization. The spill-over contribution is minimum near 0° scan angle for the 87-GHz channel and minimum near 90° for the 164–181-GHz channels. This is expected since these two channels use orthogonal linear polarizations (due to the design of the diplexer), and the feed pattern asymmetry is rotated by 90° between them. The coefficients for the polynomial fit are provided in Table I

$$T_B = c_0 + c_1\varphi + c_2\varphi^2 + c_3\varphi^3 + c_4\varphi^4. \quad (2)$$

TABLE I
SPILL-OVER COEFFICIENTS FOR TEMPEST-D
CHANNELS AT 87 AND 181 GHz

Coefficient	Units	87 GHz	181 GHz
C_0	-	1.0	1.0
C_1	- / deg	-4.99×10^{-6}	2.14×10^{-6}
C_2	- / deg ²	-4.99×10^{-7}	4.17×10^{-7}
C_3	- / deg ³	-1.69×10^{-9}	-1.70×10^{-9}
C_4	- / deg ⁴	1.07×10^{-11}	-3.87×10^{-11}

V. VALIDATION

Validation of the TEMPEST-D calibration was performed by comparing the observed T_B with coincident observations from five well-calibrated satellite microwave radiometers measuring at similar frequencies. The calibration reference sensors that were used include the Global Precipitation Measurement (GPM) mission Microwave Imager (GMI) along with four copies of the MHS on board the NOAA-19, MetOp-A, MetOp-B, and MetOp-C satellites. For the reference sensors, the intercalibrated Level 1C T_B data sets were used [3]. The Level 1C T_B data were intercalibrated to be physically consistent with GMI after accounting for sensor and view angle differences by the Precipitation Measurement Missions (PMMs) intercalibration (i.e., XCAL) team. Details of the methodology and results of these comparisons are provided in the following sections.

A. Instrument Specifications

The TEMPEST-D instrument has similar characteristics to the MHS instrument flown on board NOAA-18, NOAA-19, MetOp-A, MetOp-B, and MetOp-C. The NOAA-18 MHS failed in October 2018. Operational data from the MetOp-C MHS is only available since July 2, 2019, but this still provided 25 days of coincident observations with TEMPEST-D over the 13-month period used. For both GMI and MHS, several instrument differences must be taken into account to compare the TEMPEST-D T_B to those of the reference sensors. Frequency, bandwidth, and polarization differences must all be accounted for, as well as view angle differences for corresponding pixels. For radiative transfer model simulations, weighting functions from the end-to-end spectral response measurements [2] were used to integrate the atmospheric absorption over the instrument spectral response for each channel. Table II provides a comparison of channel characteristics for the TEMPEST-D, MHS, and corresponding GMI channels. The receiver noise of TEMPEST-D is lower than MHS, yet the resulting on-orbit NEDTs for all five channels are similar for the two sensors. The reason for this is that the scan rate of TEMPEST-D is constant, whereas the MHS scan slows across the Earth scene and accelerates through spacecraft views. This allows MHS to have a longer view of the Earth and therefore longer integration times than TEMPEST-D. The MHS integration time is 18 ms versus 5 ms for TEMPEST-D. Additional details on the TEMPEST-D instrument design and performance are available in [2].

In addition to the channel frequency and polarization differences, the GMI instrument is a conically scanning

radiometer observing at a constant zenith angle or Earth incidence angle (EIA) of $\sim 53^\circ$ for the 89-GHz channels, and $\sim 49^\circ$ for the higher frequency channels. Both the MHS and TEMPEST-D instruments are cross-track scanning radiometers with varying EIA between 0° and 60° . The cross-track scanning radiometers have rotating polarization vectors, which vary as a function of the scan angle from nadir. While the EIA is limited to similar values between the target and reference sensors, it is important to accurately model the effect of EIA-dependent differences on the observed T_B , including differences in polarization, surface emissivity, and the atmospheric slant path. As shown in Table II, both GMI and MHS have significantly different characteristics from TEMPEST-D for certain channels. These differences provide challenges in comparing the reference sensor T_B with those of TEMPEST-D, but as discussed below, there is significant value in having multiple well-calibrated reference sensors with different characteristics.

B. Validation Approach

Validation of the TEMPEST-D calibration was performed using a double-difference method [3], [4]. This approach compares observed T_B for coincident observations between the target (i.e., TEMPEST-D) and reference sensors (i.e., GMI and MHS) over nonprecipitating ocean scenes. Expected T_B differences between the sensors due to variations in channel frequency, bandwidth, view angle, and so on, are then subtracted from the observed T_B differences. The 51.6° inclination of the TEMPEST-D orbit results in regular intersections with the orbits of both the polar-orbiting NOAA/MetOp satellites and GPM. Coincident overpasses are identified that occur within a specified time window (i.e., 60 min) between the target and reference sensors. The T_B data within the intersection region are gridded and screened to eliminate land, the presence of precipitation, significant inhomogeneity within the grid box, possible sun glint, data quality issues, and so on. The input Level 1C T_B data contains data quality flags including possible sun glint. Data quality screening is also done as part of the TEMPEST-D Level 1B data processing. We also require that the zenith angle between TEMPEST-D and the reference sensors matches within 5° to reduce potential simulation errors. Fig. 4 shows an example of an orbit intersection between GPM GMI and MetOp-A MHS. The black boxes in Fig. 4 indicate $1^\circ \times 1^\circ$ grid boxes screened to eliminate those with partial coverage by either sensor and/or land contamination based on a high-resolution land mask data set. Screening for precipitation contaminated pixels is performed based on results from a 1-D variational (1-DVAR) retrieval [5]. The resulting grid-averaged T_B values for each sensor are matched with corresponding atmospheric and ocean surface parameters from the NASA GEOS-5 global data assimilation system [6]. These parameters are used as input in a radiative transfer model to account for expected sensor T_B differences for the specified ocean surface and atmospheric conditions. The atmospheric absorption is computed using the AER MonoRTM model [7]. The ocean emissivity is computed using FASTEM-6 [8], which is part of the Community Radiative Transfer Model (CRTM).

TABLE II
CHANNEL PROPERTIES OF TEMPEST-D AND THE VALIDATION REFERENCE SENSORS, INCLUDING THE MHS ON BOARD METOP-A, METOP-B, METOP-C, AND NOAA-19 AS WELL AS THE GPM GMI

Property	Sensor	89 GHz	160 GHz	183±7 GHz	183±3 GHz	183±1 GHz
Center Freq.	TEMPEST-D	87.1	164.1	173.8	178.4	180.8
	MHS	89.0	157.0	190.3	183.3±3.0	183.3±1.0
	GPM GMI	89.0	166.0	183.3+7.0	183.3+3.0	N/A
Bandwidth	TEMPEST-D	3200 MHz	3900 MHz	2232 MHz	1848 MHz	1989 MHz
	MHS	2800 MHz	2800 MHz	2200 MHz	2x1000 MHz	2x500 MHz
	GPM GMI	5865 MHz	3893 MHz	2x1874 MHz	2x1358 MHz	N/A
Polarization	TEMPEST-D	Quasi-V Pol	Quasi-H Pol	Quasi-H Pol	Quasi-H Pol	Quasi-H Pol
	MHS	Quasi-V Pol	Quasi-V Pol	Quasi-V Pol	Quasi-H Pol	Quasi-H Pol
	GPM GMI	V-Pol/H-Pol	V-Pol/H-Pol	V-Pol	V-Pol	N/A
NEΔT (K)	TEMPEST-D	0.20	0.35	0.55	0.55	0.75
	MHS	0.22	0.34	0.46	0.40	0.51
	GPM GMI	0.32	0.18	0.30	0.28	N/A
Specified Calibration Accuracy & (Precision) in Kelvin	TEMPEST-D	4.0 (2.0)	4.0 (2.0)	4.0 (2.0)	4.0 (2.0)	4.0 (2.0)
	MHS	1.0 (N/A)				
	GPM GMI	1.35 (N/A)	1.5 (N/A)	1.5 (N/A)	1.5 (N/A)	N/A (N/A)

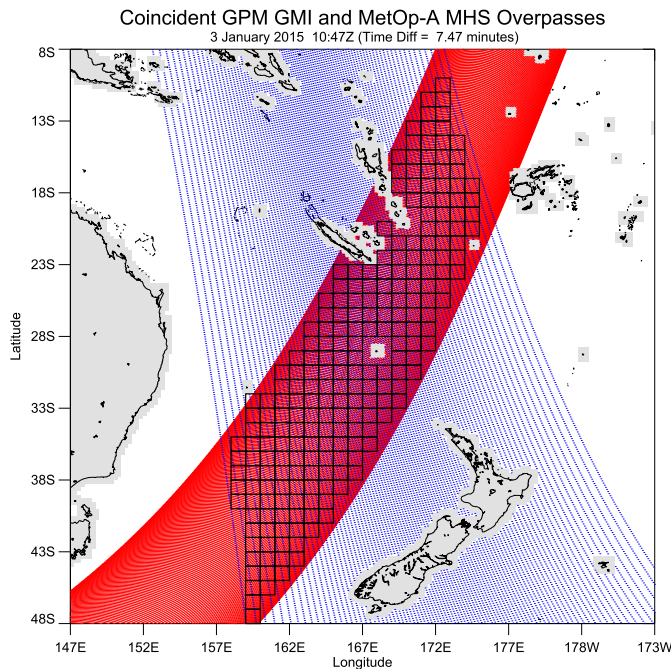


Fig. 4. Example of an orbit intersection on January 3, 2015, between GPM GMI and MHS on board MetOp-A with the corresponding $1^\circ \times 1^\circ$ grid boxes for the scan overlap region screened to remove land contamination. The red and blue dots indicate the GMI and MHS pixel locations, respectively.

Simulated T_B are computed for both the reference and target sensors by integrating over the published bandwidth for each channel (Table II), or over the spectral response weighting functions available for TEMPEST-D (Fig. 1) and GMI. The appropriate polarization and view angle for each sensor over the specified scene are also accounted for in the radiative transfer model calculations.

Fig. 5 shows an example of a coincident scene between the 183.31 ± 1 -GHz channel on MetOp-A MHS and the 180.8-GHz

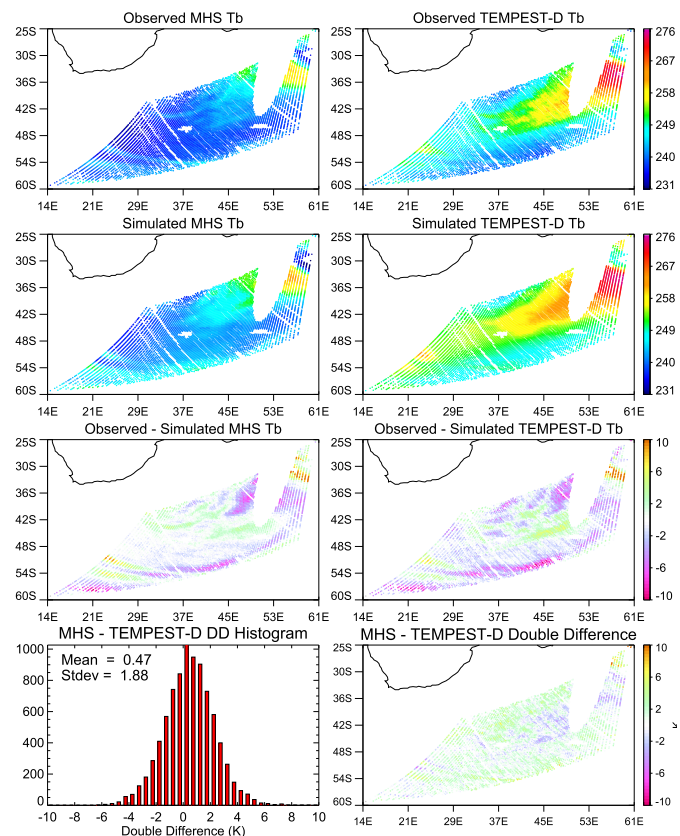


Fig. 5. Example of (Top row) observed, (Second row) simulated, and (Third row) T_B differences for coincident overpasses from December 1, 2018, between the 183 ± 1 -GHz channel on (Left) MetOp-A MHS and the 180.8-GHz channel on (Right) TEMPEST-D. (Bottom row) Resulting double-differences for the scene, along with a histogram of the values.

TEMPEST-D channel. There are significant differences in the observed T_B between MHS (top left) and TEMPEST-D (top right); however, the simulated T_B show comparable

differences primarily due to the frequency difference between the two channels. There are also significant differences between the observed (top row) and simulated T_B (second row) for each sensor, as shown in the third row, although the patterns are similar since errors in the GEOS-5 geophysical parameters and radiative transfer models have similar impacts on the two channels. As a result, the double-difference largely cancels the impact of the instrument and view angle differences as well as errors in the geophysical parameters and/or radiative transfer models, providing a result that is very consistent across the scene (bottom right). A histogram of the double differences (bottom left) shows that there is significant variability in the double difference values, but with a relatively Gaussian distribution. Errors in the double differences are more significant in the lower frequency channels, which are sensitive to ocean emissivity variations. The results over a large number of scenes, however, tend to be relatively stable.

C. TEMPEST-D Calibration Accuracy and Precision

Validation of satellite calibration by comparing with observations from reference sensors typically requires a significant time period of corresponding observations. Intercalibration of microwave imagers and sounders with the GPM GMI radiometer by the PMM XCAL team utilized six months to a year or more of corresponding data [3]. For TEMPEST-D, validation was originally performed using data from 21 days over a ~ 3 1/2 month period from October 15, 2018 to January 25, 2019. This has been subsequently extended to 50 days through November 17, 2019. Only days with nearly complete global coverage were used for the validation analysis. Although the TEMPEST-D instrument has been operating almost continuously since September 11, 2018, due to the limited capacity for downloading data to the single ground station at NASA Wallops, Wattsville, VA, USA, along with communication issues and special satellite operations, nearly complete daily global coverage from TEMPEST-D is available only 10%–20% of the time. The T_B data files used in this analysis, along with global quick look images, are publicly available at <https://tempest.colostate.edu/data>. The locations of the coincident satellite overpasses between TEMPEST-D and the five reference sensors as well as the days used in the validation analysis are shown in Fig. 6.

The panels on the left side of Fig. 7 show scatter density plots of TEMPEST-D calibration double differences with respect to the MHS reference sensors, composited using NOAA-19, MetOp-A, MetOp-B, and MetOp-C results for each of the five channels. The panels on the right side of Fig. 7 show the corresponding double-difference results by channel with respect to GPM GMI. Each point in this density plot is from a collocated $1^\circ \times 1^\circ$ grid box that has been screened for land, precipitation, etc., as described above. The variability of the double-difference estimates is due to a number of factors including errors in the geophysical parameters from the NASA GEOS-5 model, errors in the radiative transfer model, and inhomogeneity within the scene.

To obtain a sufficient number of samples to generate stable statistics, a relatively large 60-min time window is used to

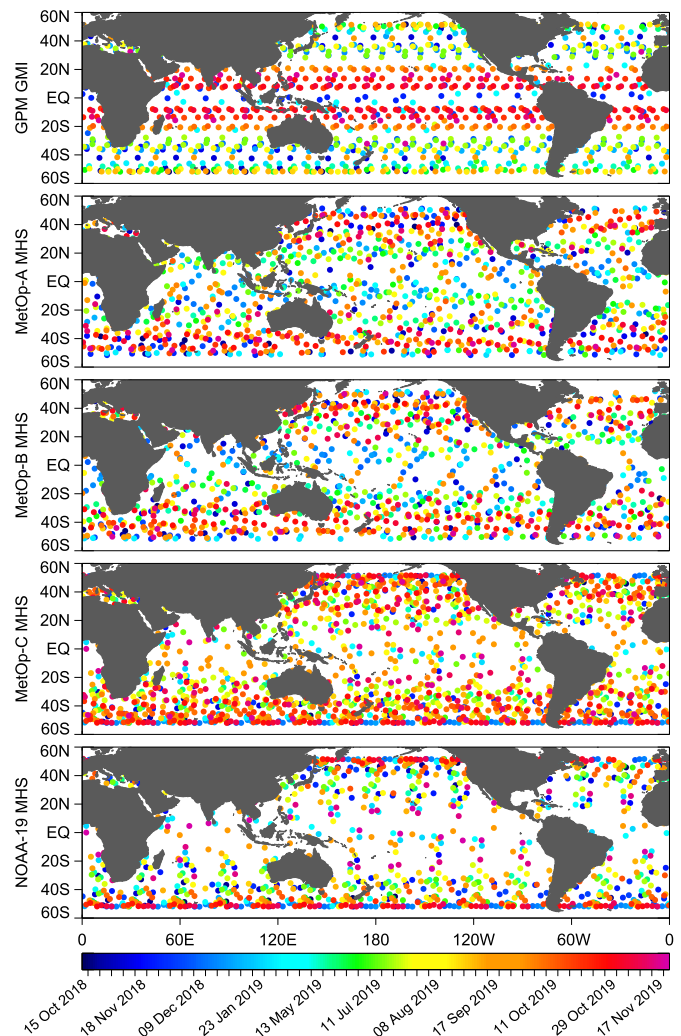


Fig. 6. Locations of coincident observations between TEMPEST-D and the five reference sensors for 50 days of relatively complete global coverage over a 13-month period from October 15, 2018 to November 17, 2019.

define temporal coincidence between the reference and target observations. While this adds meteorological noise to the individual double differences shown in Fig. 7 and, therefore, increases the scatter, it does not significantly change the mean difference values. The additional collocated double difference estimates enable stratifying the results to investigate issues including calibration stability over time and as a function of instrument temperature. As long as errors such as those mentioned above are random, estimates of the mean calibration differences are quite stable given sufficient statistics. More significant than random errors, however, are potential biases due to regional variability in the double difference estimates.

The density plot for the 164-GHz channel with respect to MHS, shown in the second row of the left-hand column in Fig. 7, shows a significant slope or scene-temperature dependence in the double differences. This is due to either an instrument calibration issue or errors in the simulated T_B for the two instruments. In the case of the 164-GHz channel, TEMPEST-D has a center frequency near 164.1 GHz versus 157.0 GHz for MHS. In addition, the polarizations

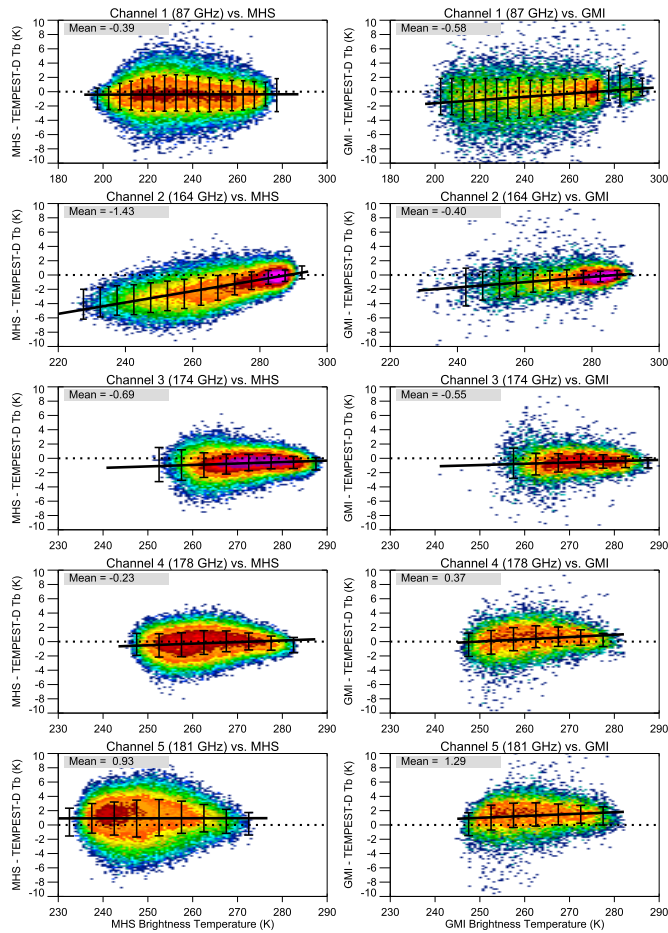


Fig. 7. Density plots of observed minus simulated double differences for individual $1^\circ \times 1^\circ$ grid boxes as a function of the observed T_B . (Left) Composite results for each of the five channels using the MHS reference sensors (MetOp-A, MetOp-B, MetOp-C, and NOAA-19), and (Right) results based on GPM GMI as the reference sensor. Results are based on 50 days of collocated data over the period from October 15, 2018 to November 17, 2019. The mean and standard deviation over 5° MHS or GMI T_B bins (x -axis) are indicated by the black solid lines and associated error bars.

for these two channels are orthogonal to each other, quasi-horizontal for TEMPEST-D and quasi-vertical for MHS. Since this channel is on the limb of the 183-GHz water vapor line where the atmosphere is not normally opaque, it has significant sensitivity to the ocean surface. These differences in polarization and frequency thus result in larger differences, and thus larger uncertainties, in the simulated T_B for this channel. The corresponding results using GMI as the reference, shown in the second row of the right-hand column in Fig. 7, also indicate a slope with scene temperature, although it is smaller, and the mean double difference is much closer to zero at -0.40 versus -1.43 for the MHS-based results. The GMI center frequency is 166.0 GHz, which is closer to that of the 164.1-GHz TEMPEST-D channel. In addition, the GMI V-Pol and H-Pol channels were combined to better match the rotating polarization of the TEMPEST-D channel. The result of these differences supports the conclusion that the scene-temperature dependence between MHS and TEMPEST-D for this channel is due in large part to simulation errors. This is

TABLE III
MEAN CALIBRATION DIFFERENCES BY REFERENCE SENSOR AVERAGED OVER 50 DAYS OF TEMPEST-D OBSERVATIONS

Reference Sensor	87 GHz	164 GHz	174 GHz	178 GHz	181 GHz
GPM GMI	-0.58	-0.40	-0.55	0.37	N/A
METOP-A MHS	-0.39	-0.92	-0.36	0.13	1.42
METOP-B MHS	-0.37	-1.25	-0.81	-0.29	1.21
METOP-C MHS	-0.35	-1.34	-0.68	-0.30	1.14
NOAA-19 MHS	-0.43	-1.89	-0.77	-0.34	0.34
Mean (MHS only)	-0.39	-1.43	-0.69	-0.23	0.93
Mean (MHS + GMI)	-0.48	-0.91	-0.62	0.07	0.93
Standard Deviation	0.12	0.51	0.21	0.39	0.41

further supported by the fact that the TEMPEST-D 164-GHz channel shares the feed horn and diplexer, as well as much of the electronics with the other high-frequency channels (i.e., 174, 178, and 181 GHz). The PMM XCAL team has also noted larger uncertainties in ocean emissivity model estimates in the 160-GHz frequency band in analyzing calibration differences between GMI and the Advanced Technology Microwave Sounder (ATMS) on board NPP and NOAA-20. For the other channels, the double-difference values are relatively flat, with minimal scene-temperature dependence over the range of observed ocean scenes.

The mean calibration difference estimates are provided in Table III for each of the reference sensors along with the composite mean and standard deviation. The mean values are weighted by the number of observations from satellite, with MetOp-B and NOAA-19 providing more coincident observations with TEMPEST-D than the other satellites. To take advantage of, and thus minimize, the impact of biases due to reference sensor differences, the mean double-difference values are calculated as an average of the MHS and GMI-based results, while the standard deviation is calculated among all five reference sensors.

There is generally very good agreement between the five reference sensors with a couple of exceptions. For the 164-GHz channel, the mean MHS double difference is -1.43 versus -0.40 for GMI, although as noted previously we believe that the GMI result is more representative of the true calibration difference due to the better correspondence in frequency and polarization with TEMPEST-D. The other notable outlier is the double difference for the NOAA-19 183 ± 1 -GHz MHS channel versus the TEMPEST-D 181 GHz channel. This channel on NOAA-19 has experienced elevated NEDT values between 3.5 and 4.0 K since early in the mission. Due to the randomness of NEDT, the slightly elevated noise values should not significantly impact the mean daily double-difference estimate. Instead, it is likely that the difference has more to do with the prevalence of coincident observations at higher latitudes, as shown in Fig. 5, than the increased noise in this channel. As a result, we include the NOAA-19 results for this channel, which decreases the computed mean difference versus TEMPEST-D, but also increases the standard deviation and thus provides a realistic measure of the residual uncertainties in the double difference estimates. The noise in the 157-GHz channel on MetOp-A also exceeded the specification of 1.0 K in April of 2019 and has continued to rise ever since. As such,

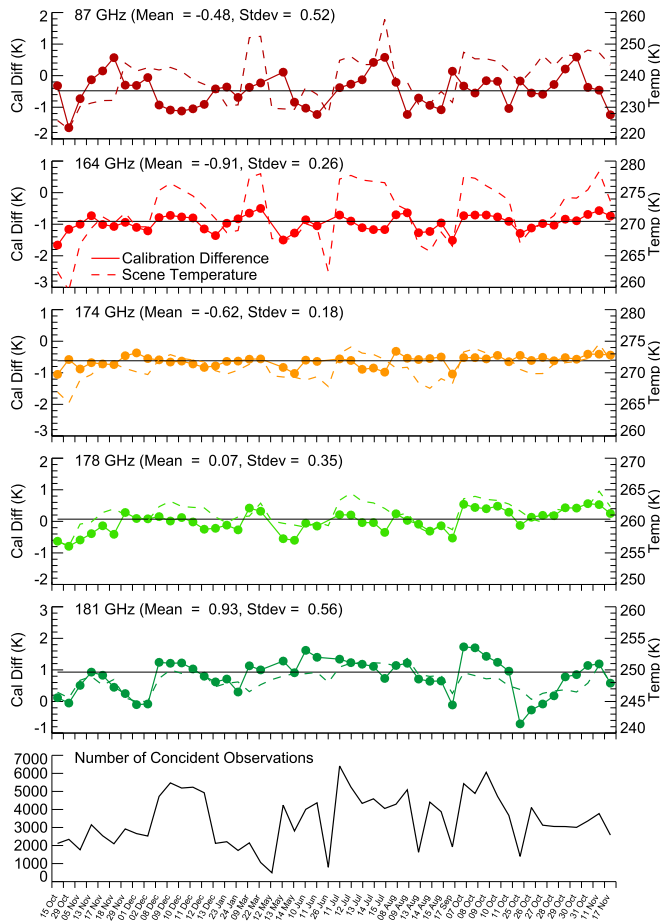


Fig. 8. Estimates of calibration differences (Reference—TEMPEST-D) composited using all five reference sensors by day. The solid lines and dots show the estimated calibration difference, and the dashed lines indicate the corresponding mean scene temperature. Each point corresponds to one day of TEMPEST-D observations. A total of 50 days of collocated data over the period from October 15, 2018 to November 17, 2019 were used.

data from this channel is not used after mid-2019 when the noise values exceeded ~ 2 K.

As shown in Table III, the mean calibration difference for all five TEMPEST-D channels is within 1 K, well within the 4-K absolute calibration requirement, and the standard deviation for the various reference sensors is within ~ 0.5 K. While there is some uncertainty in the calibration of the reference sensors, the PMM XCAL team determined that the GMI calibration was consistent with all of the MHS instruments within 0.5 K for all channels and that they are all very well calibrated and stable in an absolute sense [3], [9].

D. Calibration Stability

Fig. 8 shows estimates of daily mean calibration differences between TEMPEST-D and a composite of the five reference sensors over the 50 days of available data. The daily mean calibration difference values are indicated by the solid lines and dots, and the associated mean scene temperatures are indicated by the dashed lines. For these 50 days, nearly complete global coverage was available from TEMPEST-D, thereby providing a reasonable number of coincident scenes with the reference sensors. As noted previously, due to several issues

in downloading data to the single ground station at Wallops, the availability of days with relatively complete TEMPEST-D coverage is limited. As shown in Fig. 8, there is significant variability in the mean double-difference values over daily time scales due to limited, and highly variable, sampling. Even so, the standard deviation of the daily mean values is less than 0.51 K for all channels. Averaging the results over 15 days (not shown) results in maximum differences of less than 0.5 K for all channels, which reduces to less than 0.35 K when averaged over 25 days, thus indicating the stability of the mean calibration estimates in Table III for the 50-day period analyzed. There is also no evidence of significant calibration drifts or changes over time. TEMPEST-D is still operating, and we are continuing to collect data to monitor ongoing calibration stability.

Fig. 9 shows the calibration double differences as a function of instrument temperature. A heater is used to keep the temperature within a relatively narrow range, turning on when the instrument temperature drops below 2°C (275 K) and turning off when the temperature exceeds 4°C (277 K). With rare exceptions, the instrument temperature varies from 275 to 301 K. The instrument is turned off if the temperature exceeds 40°C (313 K), although that situation has not occurred during the mission to date. The dashed lines in Fig. 9 show the number of observations within each 2° instrument temperature bin, indicating that the majority of the samples are within an even narrower temperature range from 278 to 286 K. There are relatively few samples outside of this narrow instrument temperature range, and therefore, the corresponding double differences have larger uncertainties due to limited sampling. In any case, all five channels exhibit consistent calibration differences across the full range of observed instrument temperatures. Note that the small increase in the double difference values for the 87-GHz channel for instrument temperatures above 291 K corresponds to a very small number of points. Since fluctuations in the instrument temperature are primarily due to changes in solar illumination/heating, this also indicates that there are no significant calibration issues due to transitions into or out of the Earth's shadow, or with solar beta angle. For the TEMPEST-D orbit, the solar beta angle oscillates from minimum values of -30° to -75° to maximum values of 30° – 74° approximately every 60 days.

E. Calibration Consistency Across Track

As discussed in Section III, estimates of cross-track variations in the antenna spillover were made using data from a pitch maneuver performed on orbit. These corrections, which were on the order of a few tenths of a kelvin for all channels, were applied in calculating the T_B from the T_A . Cross-scan variations (not shown) do occur in the double difference values as a function of scan position for the lower frequency channels (i.e., 87 and 164 GHz); however, previous comparisons between MHS and ATMS suggest that these are largely due to radiative transfer model errors. Such cross-scan variations are not observed in the higher frequency channels near the 183-GHz water vapor line, which have little or no sensitivity to changes in surface emissivity as a function of

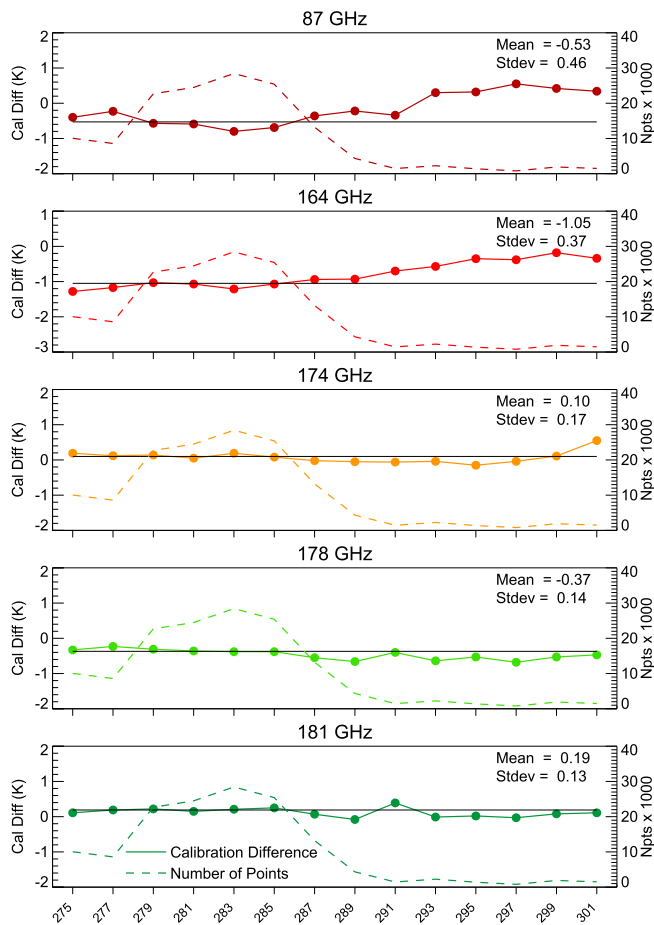


Fig. 9. Estimates of calibration differences (Reference—TEMPEST-D) as a function of instrument temperature. The results are based on matchups over the 13-month period using all five reference sensors. The solid lines show the estimated calibration difference, and the dashed lines indicate the number of observations within each 2° instrument temperature bin, as indicated by the axis on the right-hand side of the plot.

view angle. Limiting the range of allowable EIA values to near nadir increases the noise in the results due to sampling, but it does not significantly change the estimated mean calibration differences in Table III.

VI. CONCLUSION

Validation of the TEMPEST-D T_B was performed by comparing with coincident observations from five well-calibrated satellite reference sensors including GPM GMI and MHS on board MetOP-A, MetOp-B, MetOp-C, and NOAA-19. Based on data from 50 different days over a ~ 13 -month period, the mean calibration differences with respect to the reference sensors are less than 1 K, which is significantly better than the absolute calibration requirement of 4 K. Somewhat larger values as well as apparent scene-temperature-dependent differences for the 164 GHz channel versus MHS are likely the result of errors in the simulated or expected T_B differences, with the actual difference being closer to the estimated calibration difference of -0.40 with respect to GPM GMI. The standard deviation of the calibration differences with respect to the five reference sensors as well as over time using daily-mean composite estimates for all five channels is less than 0.6 K.

Using the standard deviation of the intersatellite and daily mean values as an estimate of the precision gives a substantial margin compared to the 2-K precision requirement. There is also no evidence of significant calibration changes with instrument temperature for any of the TEMPEST-D channels.

Consistency in the calibration differences as a function of scene temperature is also extremely good for all except the 164-GHz channel versus MHS. For the 87-, 174-, 178-, and 181-GHz channels, the scene temperature dependence, or slope of the estimated calibration differences, is less than 1 K, which is less than the standard deviation of the bin-averaged estimates. For the 164-GHz channel, regional variability in the double difference estimates is associated with significant differences in the simulated T_B between TEMPEST-D and the MHS reference sensors. This is due to a combination of sensitivity to the ocean surface emissivity and instrument channel differences, including significant center frequency differences and orthogonal channel polarizations. The PMM XCAL team found similar issues with large residual radiative transfer model errors impacting intercalibration estimates of the 165.5-GHz channel of the ATMS instruments on board NPP and NOAA-20 versus GPM GMI. It is believed that errors in the ocean surface emissivity estimates between 90 and 183 GHz are largely responsible for scene-temperature-dependent calibration difference estimates. This is primarily a factor for channels with significant sensitivity to the ocean surface away from the 183-GHz water vapor line along with frequency, polarization, and view angle differences between the target and reference sensors.

The on-orbit assessment of the TEMPEST-D calibration based on multiple well-calibrated reference sensors indicates that the absolute calibration accuracy is within 1 K for all channels, well within the 4-K requirement. Calibration precision, or stability over time, is within 0.6 K for all channels, also well within the 2-K requirement. While the TEMPEST-D radiometer is substantially smaller, lower power, and lower cost than similar operational radiometers, it has comparable performance in terms of instrument noise, calibration accuracy, and calibration stability/precision. The performance of the advanced technology employed in the TEMPEST-D instrument design suggests that such a small, low-cost satellite, and instrument is potentially suitable for a wide range of Earth science applications.

ACKNOWLEDGMENT

The authors would like to acknowledge the Temporal Experiment for Storms and Tropical Systems—Demonstration (TEMPEST-D) Team, Blue Canyon Technologies (BCT), Lafayette, CO, USA, who built and operate the TEMPEST-D satellite bus. They would also like to thank NASA Wallops, Wattsville, VA, USA, for providing ground station services and support. They would also like to acknowledge and thank Pamela Millar and Robert Bauer of NASA's Earth Science Technology Office, NASA Goddard Spaceflight Center, Greenbelt, MD, USA, who managed the grant on behalf of the NASA's Earth Venture Technology Program. Portions of this work were performed at the NASA Jet Propulsion Laboratory, California Institute of Technology, Pasadena, CA, USA.

REFERENCES

- [1] S. Padmanabhan *et al.*, "Radiometer payload for the temporal experiment for storms and tropical systems technology demonstration mission," in *Proc. IEEE Int. Geosci. Remote Sens. Symp. (IGARSS)*, Fort Worth, TX, USA, Jul. 2017, pp. 1213–1215, doi: [10.1109/IGARSS.2017.8127176](https://doi.org/10.1109/IGARSS.2017.8127176).
- [2] S. Padmanabhan *et al.*, "TEMPEST-D radiometer: Instrument description and pre-launch calibration," *IEEE Trans. Geosci. Remote Sens.*, to be published.
- [3] W. Berg *et al.*, "Intercalibration of the GPM microwave radiometer constellation," *J. Atmos. Ocean. Technol.*, vol. 33, no. 12, pp. 2639–2654, Dec. 2016, doi: [10.1175/JTECH-D-16-0100.1](https://doi.org/10.1175/JTECH-D-16-0100.1).
- [4] W. Berg, R. Kroodsma, C. D. Kummerow, and D. S. McKague, "Fundamental climate data records of microwave brightness temperatures," *Remote Sens.*, vol. 10, no. 8, p. 1306, Aug. 2018, doi: [10.3390/rs10081306](https://doi.org/10.3390/rs10081306).
- [5] D. I. Duncan and C. D. Kummerow, "A 1DVAR retrieval applied to GMI: Algorithm description, validation, and sensitivities," *J. Geophys. Res., Atmos.*, vol. 121, no. 12, pp. 7415–7429, Jun. 2016, doi: [10.1002/2016JD024808](https://doi.org/10.1002/2016JD024808).
- [6] A. Molod, L. Takacs, M. Suarez, J. Bacmeister, I.-S. Song, and A. Eichmann, "The GEOS-5 atmospheric general circulation model: Mean climate and development from MERRA to Fortuna," Global Model. Data Assimilation, NASA Goddard Space Flight Center, Greenbelt, MD, USA, NASA Tech. Rep. NASA TM-2012-104606, 2012, vol. 28, p. 117. [Online]. Available: <https://gmao.gsfc.nasa.gov/pubs/docs/Molod484.pdf>
- [7] S. A. Clough *et al.*, "Atmospheric radiative transfer modeling: A summary of the AER codes," *J. Quant. Spectrosc. Radiat. Transf.*, vol. 91, no. 2, pp. 233–244, 2005, doi: [10.1016/j.jqrst.2004.05.058](https://doi.org/10.1016/j.jqrst.2004.05.058).
- [8] M. Kazumori and S. J. English, "Use of the ocean surface wind direction signal in microwave radiance assimilation," *Quart. J. Roy. Meteorol. Soc.*, vol. 141, no. 689, pp. 1354–1375, Apr. 2015, doi: [10.1002/qj.2445](https://doi.org/10.1002/qj.2445).
- [9] F. J. Wentz and D. Draper, "On-orbit absolute calibration of the global precipitation measurement microwave imager," *J. Atmos. Ocean. Technol.*, vol. 33, no. 7, pp. 1393–1412, Jul. 2016, doi: [10.1175/JTECH-D-15-0212.1](https://doi.org/10.1175/JTECH-D-15-0212.1).



Wesley Berg (Member, IEEE) received the B.S., M.S., and Ph.D. degrees in aerospace engineering from the University of Colorado, Boulder, CO, USA, in 1988, 1989, and 1993, respectively.

He worked with the Cooperative Institute for Research in Environmental Science (CIRES), NOAA's Environmental Research Laboratories, Boulder, CO, USA. He is a Senior Research Scientist with the Department of Atmospheric Science, Colorado State University, Fort Collins, CO, USA. His research interests involve satellite remote sensing of

precipitation and other hydrologic parameters with a focus on instrument calibration and the development and analysis of satellite retrievals for long-term climate applications.



Shannon T. Brown (Senior Member, IEEE) received the B.S. degree in meteorology from Pennsylvania State University, State College, PA, USA, in 2001, and the M.S. degree in atmospheric science and the Ph.D. degree in geoscience and remote sensing from the University of Michigan, Ann Arbor, MI, USA, in 2003 and 2005, respectively.

He joined Microwave Advanced Systems Section, Jet Propulsion Laboratory (JPL), Pasadena, CA, USA, in 2005, as a member. He is a Principal Technologist with NASA JPL. He has been involved with spaceborne Topex, Jason-1, 2, and 3 Microwave Radiometers, and the WindSat Polarimetric Radiometer. He is the Principal Investigator of Compact Ocean Wind Vector Radiometer being developed for the U.S. Air Force and Instrument Scientist for the NASA Juno Microwave Radiometer on the Juno New Frontiers mission to Jupiter. His research interests include microwave radiometer system development, calibration, geophysical algorithm development for both passive and active sensors, extraction of climate data records, and radiometer science.

Dr. Brown was a recipient of the NASA Exceptional Achievement Medal in 2009, the JPL Lew Allen Award in 2010, eight NASA Group Achievement awards, and the NASA Space Act Award in 2012. He is a member of the Ocean Surface Topography Science Team, the Ocean Salinity Science Team, the SMAP Science Team, and the Juno Science Team.



Boon H. Lim received the B.S. and M.S. degrees in electrical engineering and the Ph.D. degree in geoscience and remote sensing from the University of Michigan (UMich), Ann Arbor, MI, USA, in 1999, 2001, and 2008, respectively.

He is the Project Systems Engineer and a NASA Engineering Technical Authority for PREFIRE with Jet Propulsion Laboratory, California Institute of Technology (Caltech), Pasadena, CA, USA, where he has worked on and developed a variety of instruments, including GEOSTAR, HAMSr, MTHP, and RACE, and also lecturers on aerospace engineering. He is one of the lucky few to have successfully had his instruments ground-based, airborne, and spaceborne.



Steven C. Reising (Senior Member, IEEE) received the B.S.E.E. (*magna cum laude*) and M.S.E.E. degrees in electrical engineering from Washington University in St. Louis, Saint Louis, MO, USA, in 1989 and 1991, respectively, and the Ph.D. degree in electrical engineering from Stanford University, Stanford, CA, USA, in 1998.

He served as an Assistant Professor of electrical and computer engineering with the University of Massachusetts at Amherst, Amherst, MA, USA, from 1998 to 2004, where he received tenure.

He was a Visiting Faculty Member with the University of Paris VI (Université Pierre et Marie Curie), Paris, France, during the first half of 2014. He joined Colorado State University (CSU), Fort Collins, CO, USA, in 2004, where he served as an Associate Professor from 2004 to 2011 and has been a Full Professor of electrical and computer engineering since July 2011. He is the Principal Investigator of 17 grants from NASA, NOAA, the National Science Foundation (NSF), the Department of Defense, the Office of Naval Research (ONR), NPOESS, the European Space Agency (ESA), Ball Aerospace, and First RF. He has served as a Principal Faculty Advisor for 17 M.S./Ph.D. students who have completed their degrees and work in universities, industry, and government laboratories. His research interests span a broad range of remote sensing disciplines, including microwave remote sensing of the Earth's atmosphere and oceans from airborne platforms, small satellites, and CubeSats; the design and development of radiometer systems from microwave to submillimeter-wave and THz frequencies (18–850 GHz); Lidar systems for sensing temperature and winds in the middle and upper atmosphere; and lighting-ionosphere interactions and atmospheric electrodynamics.

Dr. Reising received the NSF CAREER Award in the areas of physical and mesoscale dynamic meteorology from 2003 to 2008 and the Office of Naval Research Young Investigator Program (YIP) Award for passive microwave remote sensing of the oceans from 2000 to 2003. He has been serving as the Chair of the Ad-hoc Committee for Intersocietal Relations since 2019 and an Elected Administrative Committee (AdCom) Member of the IEEE Geoscience and Remote Sensing Society (GRSS) since 2003. He served as an Elected AdCom Member of the IEEE Microwave Theory and Techniques Society (MTT-S), from 2014 to 2019. He served as the MTT-S Inter-Society Committee Chair of IEEE from 2015 to 2018, the GRSS Vice-President of Information Resources from 2011 to 2018, and the GRSS Vice-President of Technical Activities from 2008 to 2010. He was a Founding Member of IEEE GEOSCIENCE AND REMOTE SENSING LETTERS (GRSL) Editorial Board and served as an Associate Editor from 2004 to 2013. He is a Guest Editor of three special issues and one special section of the IEEE TRANSACTIONS ON GEOSCIENCE AND REMOTE SENSING (TGRS). He served as the Immediate Past Chair of the U.S. National Committee of the International Union of Radio Science (USNC-URSI) from 2015 to 2017, the Chair from 2012 to 2014, and the Secretary from 2009 to 2011 of all ten URSI Commissions. He is a member of URSI Commissions F, G, and H, the American Meteorological Society, the American Geophysical Union, the American Association for the Advancement of Science, Tau Beta Pi, and Eta Kappa Nu.



Yuriy Goncharenko (Member, IEEE) received the B.S. and M.S. degrees from Kharkov National Polytechnic University, Kharkiv, Ukraine, in 1998 and 1999, respectively, and the Ph.D. degree in radio-physics from the Institute for Radiophysics and Electronics NAS of Ukraine, Kharkiv, in 2006.

From 2012 to 2013, he was a Fulbright Scholar with Applied Physics Laboratory, University of Washington, Seattle, WA, USA, where he focused on airborne synthetic aperture radars for remote sensing of the sea surface. He also worked with the University of Birmingham, Birmingham, U.K., on the design of signal processing algorithms for ultraprecise quantum gravity sensors. He is with the Microwave Systems Laboratory, Colorado State University, Fort Collins, CO, USA. His research interests include the design and implementation of calibration, signal processing, and target detection techniques.



Christian D. Kummerow received the A.B. degree (*cum laude*) in physics from the University of California at Berkeley, Berkeley, CA, USA, in 1982, and the Ph.D. degree in atmospheric physics from the University of Minnesota, Minneapolis, MN, USA, in 1987.

From 1997 to 2000, he was the TRMM Project Scientist at the NASA Goddard Space Flight Center, Greenbelt, MD, USA, and continues to serve on the science teams of both the TRMM as well as the recently launched Global Precipitation Mission where he leads the team responsible for the passive microwave rainfall products. He is a Professor of atmospheric science with Colorado State University, Fort Collins, CO, USA, where he also serves as the Director of the Cooperative Institute for Research in the Atmosphere. He has spent much of his career studying the global water and energy cycles. His research interests include observing the global water cycle and its uncertainties—how uncertainties relate to physical aspects of the atmosphere, and thus the fundamental processes underlying precipitation.



Todd C. Gaier received the Ph.D. degree in physics [studying the cosmic microwave background (CMB)] from the University of California at Santa Barbara, Santa Barbara, CA, USA, in 1993.

He is the Jet Propulsion Laboratory (JPL) Deputy Director of astronomy and physics, and also a JPL Fellow, a Senior Research Scientist, and a Faculty Associate of astronomy with the California Institute of Technology, Pasadena, CA, where he was previously the Chief Technologist for JPL's Astronomy and Physics Directorate and prior to that he was the Supervisor of Microwave Systems Technology Group, JPL. Projects supported by the group included the Planck-LFI mission to study the anisotropy and polarization of the CMB; the Q/U Imaging Experiment (QUIET) exploring the polarization of the CMB; GeoSTAR, an interferometric synthetic aperture imager for Earth atmospheric sounding from geostationary orbit; and the Advanced Microwave Radiometers for the Jason III mission mapping small variations in sea level across the globe monitoring conditions such as El Niño, the integrated receivers for the Juno Microwave Radiometers, the Compact Ocean Wind Vector Radiometer, a low-cost alternative to ocean wind measurement, and Temporal Experiment for Storms and Tropical Systems—Demonstration (TEMPEST-D), a CubeSat demonstrator for a mission to study temporal behavior of clouds and precipitation. His research interests include millimeter-wave electronics for applications in astrophysics and Earth remote sensing.



Sharmila Padmanabhan (Member, IEEE) received the Ph.D. degree from Colorado State University, Fort Collins, CO, USA, in 2009.

She is a Section Staff Member with Instrument Electronics and Software Section, Jet Propulsion Laboratory, California Institute of Technology, Pasadena, CA, USA. Her research interests include millimeter-wave, submillimeter-wave, and infrared instrumentation for remote sensing, calibration/validation and performance assessment of microwave radiometers, and geophysical retrieval algorithm development.